Figure Captions

Fig. 2-1

Schematic view of tandem mirror GAMMA 10; (a) magnetic coil set, (b) magnetic flux tube with heating systems, (c) axial magnetic field and potential distributions.

Fig. 3-1

Output intensities of the MCP are shown as a function of Maxwellian electron temperature T_e for the use of various X-ray absorbers noted in the figure.

Fig. 3-2

X-ray intensities with various T_e normalized by the intensities with the polypropylene combined with the 1.5 μm thick polyester absorber as a function of the thickness of the polyester.

Fig. 3-3

Co-ordinate system for tomographic reconstruction. Function $f(\kappa, \phi)$ is the line integration of source function $g(r, \chi)$ along the line L.

Fig. 4-1

Schematic view of a single channel semiconductor X-ray detector.

Fig. 4-2

(a) Schematic view of a multichannel semiconductor X-ray-detector array. (b) The theoretical results of the diffusing-charge distributions J_{sx} using Eq. (4-8) from a multichannel detector for unit-intensity X rays. X rays are injected at $x=y=0$ with the energy E from 1 to 10 keV. Here, the typical values of d_{sub}=300

μm and L=100 μm are utilized. Each channel size is denoted as x_{det} and y_{det}.

Fig. 4-3
Three dimensional and contour plots of electron distribution function (Pastukhov model: R=3, ϕ/T=5).

Fig. 4-4
(a) Schematic figure of axial potential profile. Warm electrons created at plug region coming into central cell climbing over thermal barrier potentials. (b) Velocity space at the plug region. (c) Velocity space at central cell.

Fig. 4-5
Central electron distribution function of Pastukhov model (R=1.23) and real loss boundary. The distribution satisfies the boundary conditions at the vertex and agrees well with the real loss boundary. Each contour is represented on a log scale.

Fig. 4-6
Electron velocity space at the plug. Electrons in region I pass to the central cell; those in region II are trapped in the plug/barrier mirror cell; those in III are trapped in the plug potential. Solid lines denote level curves of distribution functions for strong ECH scheme at the plug and the barrier resonance layer.

Fig. 5-1
(a) The magnetic coil and magnetic flux tube in the GAMMA 10 tandem mirror along with semiconductor X-ray detector locations and the viewing lines of sight labelled with C and A in the central cell and anchor region, respectively. (b) Schematic drawings of a newly proposed matrix-type semiconductor detector for measuring temporally and spatially resolved T_e during a single plasma

discharge alone. The detector consists of six rows having different thicknesses of thin dead layers (SiO_2) with 1, 15, 242, 1, 110, and 495 nm [see each matrix row labelled from (i) to (vi), respectively]. These layers are proposed as ultra thin "X-ray absorbers" with different thicknesses. Each row has seven channels (columns) for X-ray tomographic reconstructions. The depletion layer thicknesses d_{dep} range 21.9 μm for the first three rows and 28.9 μm for the remainder. The diffusion length in the field-free substrate region ranges 150 μm. A 300 μm thick n-type silicon wafer is utilized. (c) The detector response of each labelled detector row in (b) normalized by the incident X-ray energy is plotted, respectively. Here, the effects of the detector response and the absorption effects of a 160 nm thick aluminium layer for cutting out visible light, as well as the "SiO_2 X-ray absorber", are totally included. For the anchor X-ray observations, a sixteen channel semiconductor detector array having d_{dep} of 20 μm, and an 8 nm thick dead layer with a 0.5 μm thick polymer filter is employed. The X-ray response is plotted with the dotted curve in (c).

Fig. 5-2

Temporal evolution of the radial profiles of line-integrated X-ray brightness. The data from the two different detector rows are simultaneously observed in the central cell of GAMMA 10. For the energy responses of the data (a) and (b), one may refer to the thick-solid and the dashed curves in Fig. 5-1(c), respectively.

Fig. 5-3

Temporal evolution of spatially resolved T_e using a single plasma discharge alone. The data in Fig. 5-2 from the matrix detector are employed for the tomographically reconstructed data analyses.

Fig. 6-1

Temporal evolution of diamagnetisms in (a) the anchor $\Delta\Phi_a$ and (b) the central cell $\Delta\Phi_c$, as well as the X-ray detector signals viewing through r_c=130 mm with a 15 and a 110 nm thick "SiO_2 filter" in the central cell Isx_c in (c) and (d), respectively, and (e) in the anchor region Isx_a mapped at r_c=100 mm along the magnetic flux tube. At t=110 ms, cold gas puffing alone from an anchor NBI port without fast neutral beams is incident into ICH produced anchor hot ion plasmas with T_i of a few keV. After about 130 ms, sawtooth oscillations appear in the X-ray signals.

Fig. 6-2

Sawtooth oscillations appearing in the X-ray signals in figures 6-1(c) and (d) are expanded during the period of t=130-140 ms. A more detailed data set of the temporal evolution of the central cell X-ray signals Isx_c at r_c=-130, -87, -43, 0, 43, 87, and 130 mm is shown in 6-2(a)-(g), respectively. Here, data from the detector row of (ii) in figure 5-1(b) are displayed. Note the difference of phase in the sawtooth signals. For instance, at $t=t_1$ (135.20 ms), the peak of the oscillatory amplitude appears in (b), while the bottom in (g). Similarly, the inverse phase relation is found at $t=t_2$ (135.32 ms) for the signals in (b) and (g). The sign of plus for r_c is defined as the direction of the upper side from the midplane (r_c=0).

Fig. 6-3

Temporal variation of the central cell X-ray radial profiles obtained from the detector row of (ii) in figure 5-1(b). An oscillatory motion of the peak positions of the X-ray brightness profiles with time is highlighted with the thick solid curve.

Fig. 6-4

Tomographically reconstructed six central cell X-ray profiles are shown in figures 6-4(a)-(f) at t=110.00, 138.92, 139.01, 139.10, 139.19, and 139.28 ms, respectively. Here, the data from the matrix row of (v) in figure 5-1(b) are utilized. The rotational motion of the peak positions is clearly found in these three-dimensional plots as well as their contour mappings in (b)-(f), showing a half cycle of the rotation from t=138.92 to 139.28 ms. Here, the locations of P, Q, R, and S are defined in each figure (see figure 6-7).

Fig. 6-5

The three-dimensional displays of bulk T_e are obtained by the use of the same single plasma discharge (figure 6-4) having sawtooth oscillations. X-ray data from the various matrix rows including the data in figures 6-4(a)-(f) are utilized for the T_e analyses. Each contour represents T_e=10, 30, 50, 70, and 90 eV. Two data sets during (i) the unstable sawtooth period from t=138.92 to 139.28 ms (see figures 6-1, 6-2, and 6-4) and (ii) the stable duration from t=110.00 to 110.35 ms are shown.

Fig. 6-6

The profiles of T_e at $t= t_0$ (open circles) as well as after $t= t_3$ (filled circles) in figures 6-4 and 6-5 (i.e. before and after the oscillations) are compared.

Fig. 6-7

Temporal evolution of the central cell X-rays viewing through the locations of (a) P, and (d) S [see again figure 6-4 for the locations of P (r_c=-130 mm) and S (r_c=130 mm)]. End loss ions flowing along the magnetic lines of force connected from the locations of (b) Q (r_c=-112 mm), and (c) R (r_c=-112 mm) (figure 6-4) are plotted. As shown in figure 6-4, the positions of P, Q, R, and S locate in an

anti-clockwise direction (the $\boldsymbol{E}\times\boldsymbol{B}$ rotational direction). After the oscillations start, oscillatory behaviour in the end loss ion signals then begins to appear in (b) and (c). The signal peaks in (a)-(d) successively appear [see the successive peaks from $t=t_3$ to t_7 in (a)-(d)]. These signals provide a consistent picture of the plasma rotation in figures 6-4 and 6-5. In addition to the data in figures 6-4 and 6-5, the data set in this figure gives information on the whole plasma rigid rotation all through the GAMMA 10 plasma column from the central cell to the end region.

Fig. 6-8

(a) The central cell X-ray matrix detector signal is replotted [see figure 6-1(c)] for physics interpretations of the rotational motion in figures 6-4, 6-5 and 6-7. Temporal evolution of (b) the frequency of the oscillation, f_0, in (a), and the tip value of the parabolically shaped central potential, Φ_{C0}, by the use of a heavy ion beam probe is plotted. The matrix detector provides (d) the peaked value of the T_e profile, T_{e0}, traced with time during the single discharge. In (e), some typical data points in f_0 at t=130.58, 132.30, 136.23, and 138.35 ms are plotted as a function of $-(\mathrm{d}\Phi_C/\mathrm{d}r)/r$, which is a representative parameter of an $\boldsymbol{E}\times\boldsymbol{B}$ rotational frequency at each r. Here, r denotes the distance from the peak position of Φ_C. The data at three radial locations of r=4, 9, 13 cm are marked with the open and filled circles, and square, respectively, at each time.

Fig. 6-9

The open circles represent various combinations of the central cell diamagnetism $\Delta\Phi_c$ and the anchor diamagnetisms $\Delta\Phi_a$ in the cases of stable plasmas. The existence of the boundary for maintaining stable plasmas is highlighted with the thin solid line. The temporal evolution of the diamagnetisms in figure 6-1 from 130 to 140 ms is superimposed with a thick solid curve (i.e. continuous filled circles) along with the notes of the

diamagnetism relations at $t=t_0$, t_1, and t_7 in figures 6-2, 6-4 and 6-5. The remarkable growth of the plasma oscillations after around $t=t_1$ (figure 6-1) agrees well with the time when the thick solid curve approaches ($t=t_1$) and almost crosses ($t=t_7$) the stability boundary. In these experiments, beta values in the plug and barrier regions are sufficiently smaller than those in the central cell and the anchor regions.

Fig. 6-10
Temporal evolution of the central cell X-ray radial profiles obtained from the detector row having 15-nm-thick dead layer.

Fig. 6-11
(a) and (b) show the tomographically reconstructed X-ray profiles at t=105 ms and t=115 ms in Fig. 6-10 (i.e. before and after the central ECH injections, respectively). In (c), the value of T_e at t=105 ms and t=115 ms are compared by the use of the filled and open circles, respectively. As one can see by the X-ray increase during the injection period of the central ECH in Fig. 6-10, the analyzed value of T_e, in fact, increase by 30% due to the central ECH. In (d), the scaling of T_e with electron-confining thermal-barrier potentials ϕ_b on the magnetic axis are plotted. The value of T_e before and after the central ECH are compared by the use of the filled and open circles, respectively. The thick-solid and dashed curves show the theoretical results from the power balance equation (6-1) with the use of the energy confinement time from the generalized Pastukhov's theory modified by Cohen et al. These curves are calculated with the warm-electron temperatures T_{ew}=1 keV, and its ratio of n_{ew}/n_c=0.1% to the central-cell density $n_c=2\times10^{18}$ m^{-3}, and T_i=1 keV.

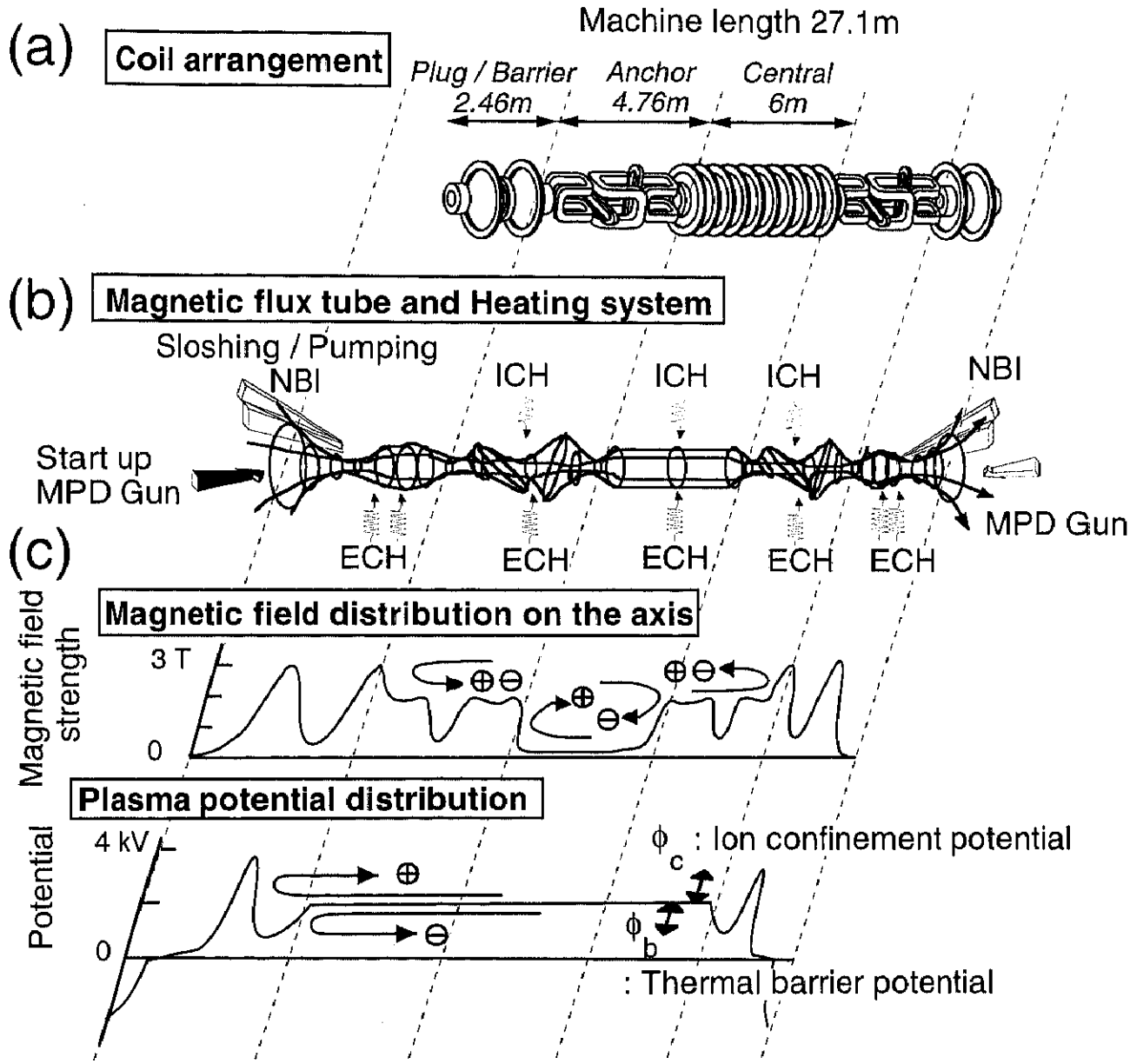
(a)
Coil arrangement
Machine length 27.1m
Plug / Barrier
2.46m
Anchor
4.76m
Central
6m
(b)
Magnetic flux tube and Heating system
Sloshing / Pumping
NBI
ICH
ICH
ICH
NBI
Start up
MPD Gun
MPD Gun
ECH
ECH
ECH
ECH
ECH
(c)
Magnetic field distribution on the axis
Magnetic field strength
3 T
0
Plasma potential distribution
Potential
4 kV
0
ϕ_c : Ion confinement potential
ϕ_b
: Thermal barrier potential

Fig. 2-1

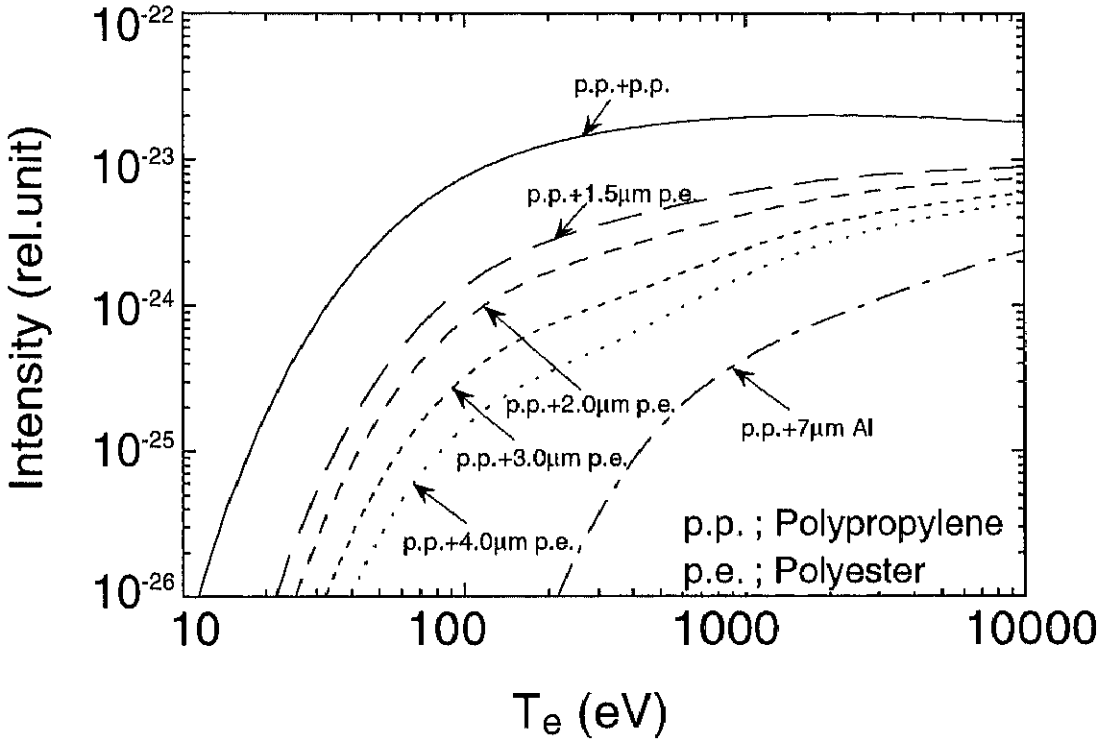
Intensity (rel.unit)
10-22
10-23
10-24
10-25
10-26
10
100
1000
10000
Te (eV)
p.p.+p.p.
p.p.+1.5μm p.e.
p.p.+2.0μm p.e.
p.p.+3.0μm p.e.
p.p.+4.0μm p.e.
p.p.+7μm Al
p.p. ; Polypropylene
p.e. ; Polyester

Fig. 3-1

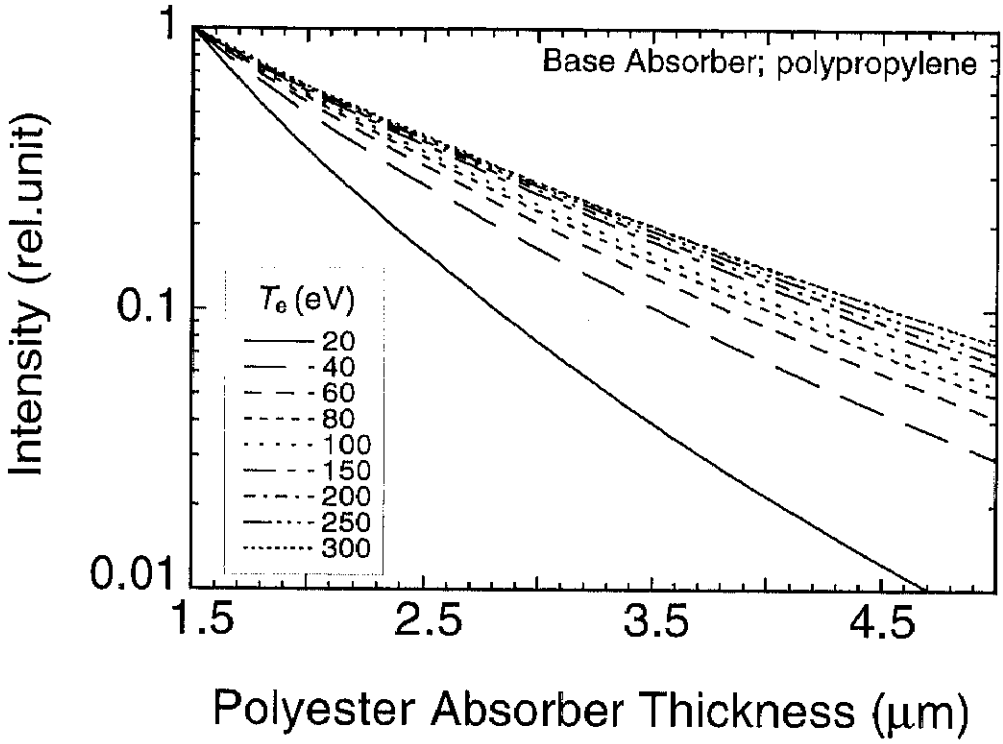
Base Absorber; polypropylene
T_e (eV)
20
40
60
80
100
150
200
250
300
Intensity (rel.unit)
1
0.1
0.01
1.5
2.5
3.5
4.5
Polyester Absorber Thickness (μm)

Fig. 3-2

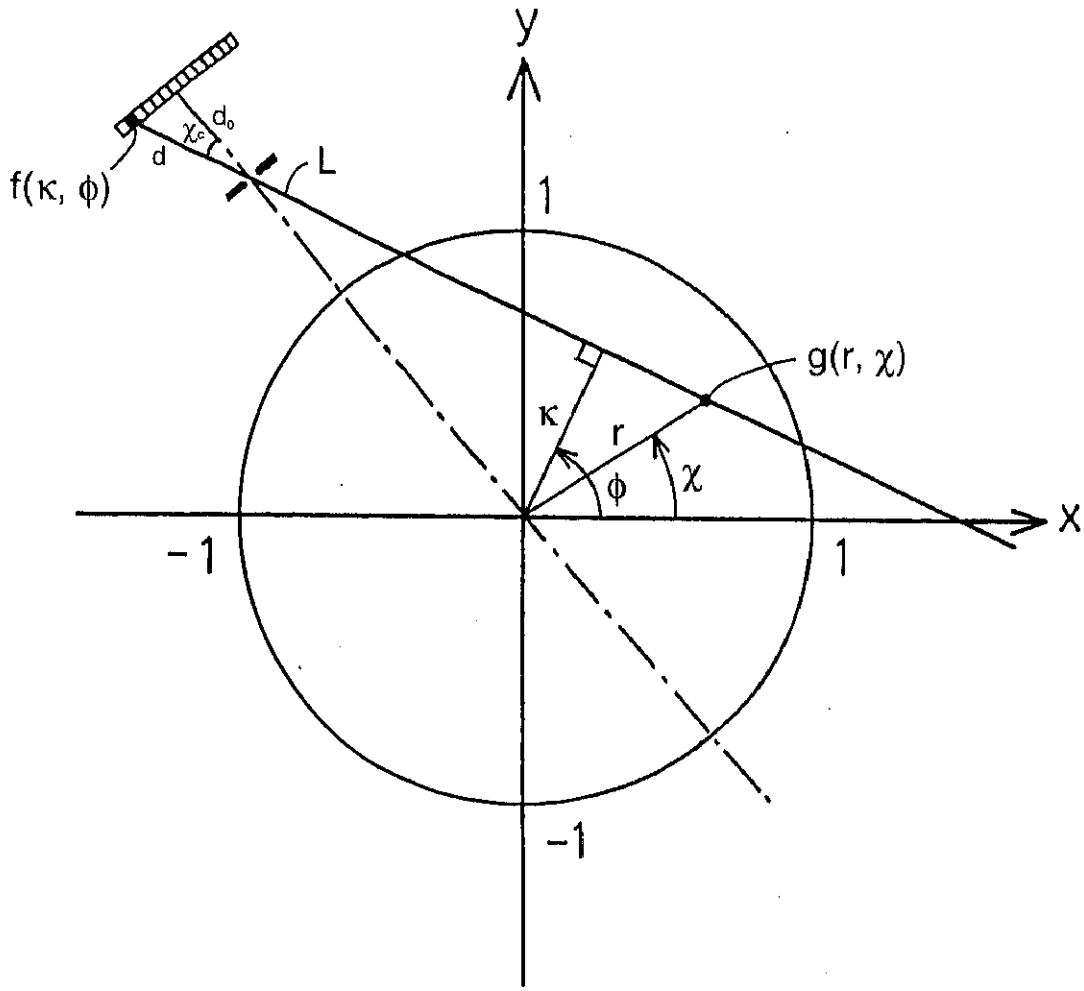

Fig. 3-3

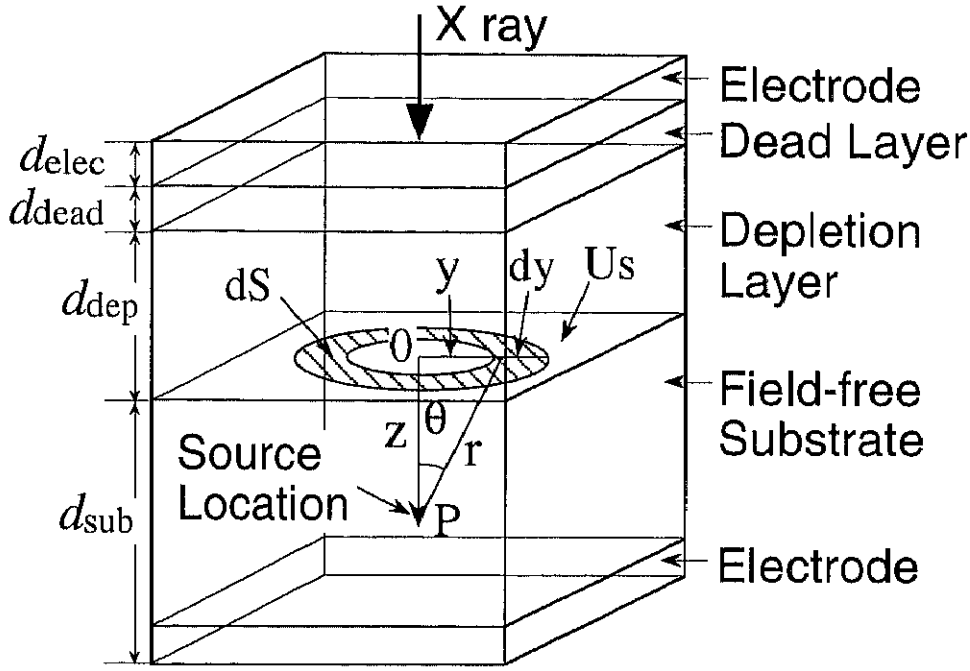
X ray
Electrode
Dead Layer
Depletion Layer
Field-free Substrate
Electrode
d_{elec}
d_{dead}
d_{dep}
d_{sub}
dS
y
dy
Us
0
z
θ
r
Source Location
P

Fig. 4-1

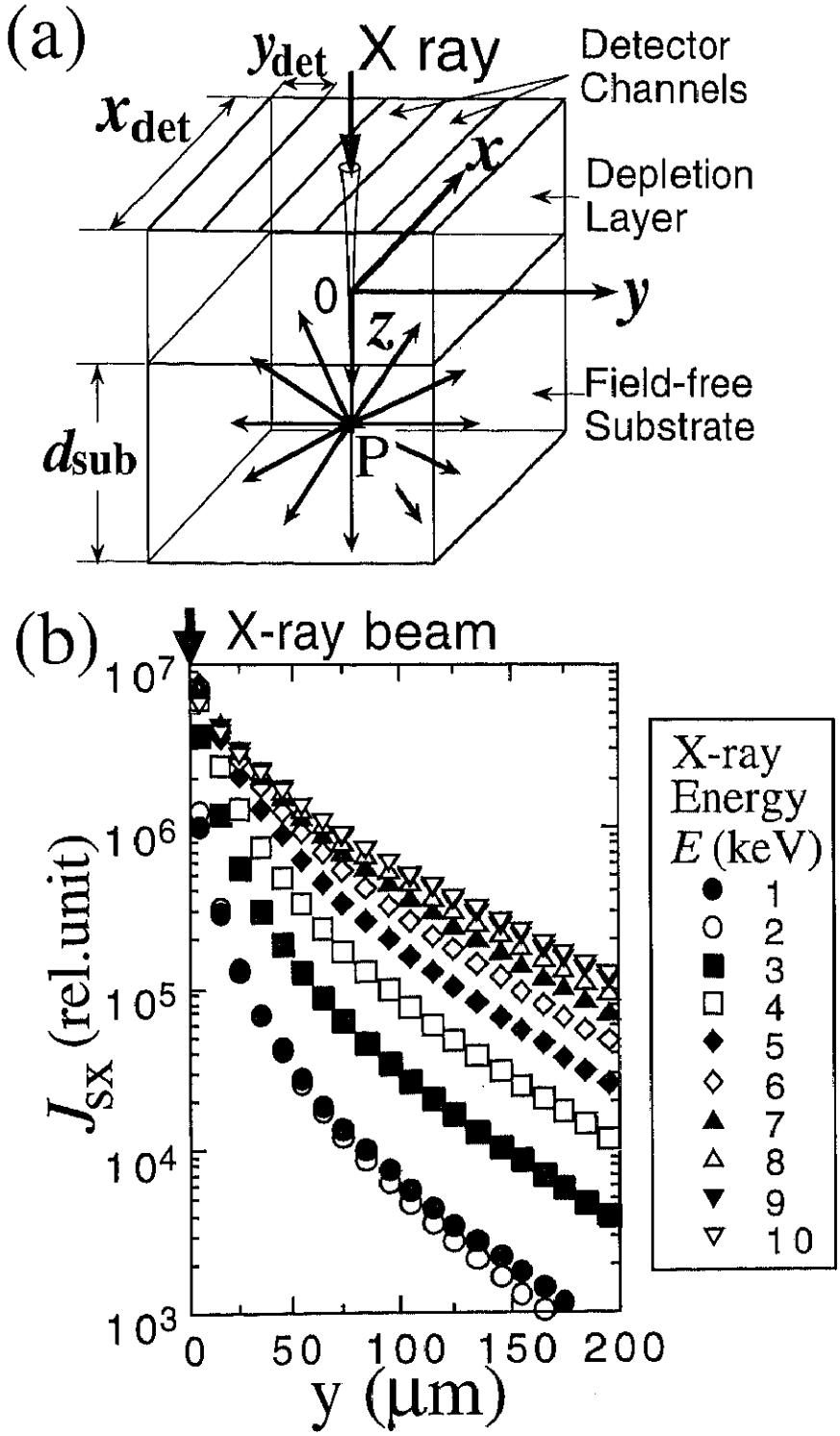
(a)
y_{det}
X ray
Detector Channels
x_{det}
x
Depletion Layer
0
y
z
Field-free Substrate
d_{sub}
P
(b)
X-ray beam
10^7
10^6
10^5
10^4
10^3
J_{sx} (rel.unit)
0
50
100
150
200
y (μm)
X-ray Energy E (keV)
1
2
3
4
5
6
7
8
9
10

Fig. 4-2

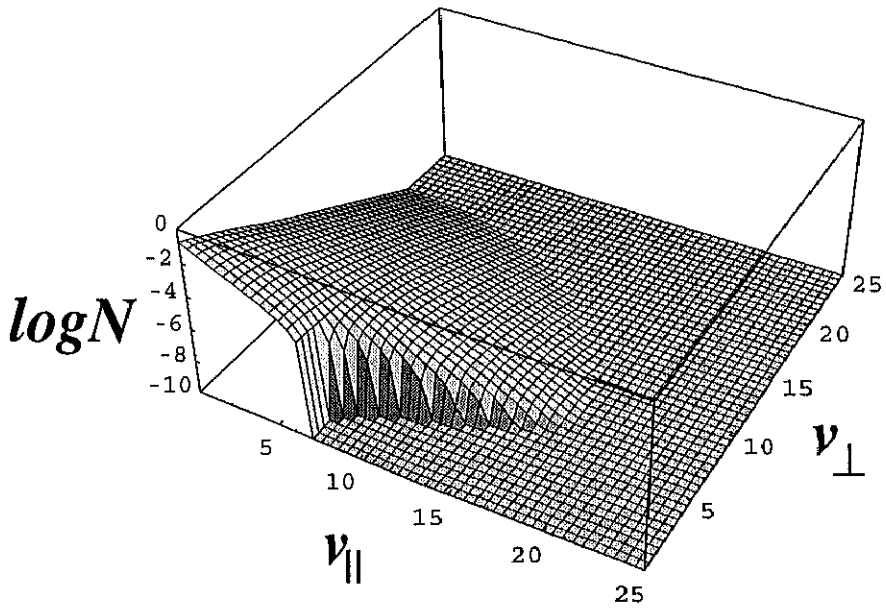
logN
0
-2
-4
-6
-8
-10
5
10
15
20
25
$v_{||}$
25
20
15
10
5
$v_{\perp}$

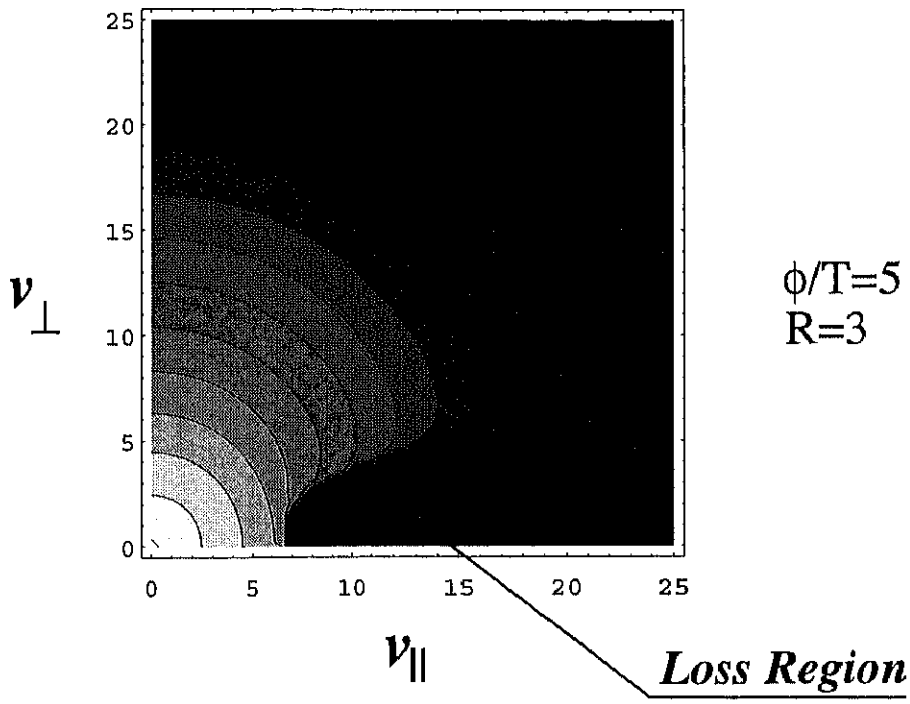
25
20
15
10
5
0
$v_{\perp}$
0
5
10
15
20
25
$v_{||}$
ϕ/T=5
R=3
Loss Region

Fig. 4-3

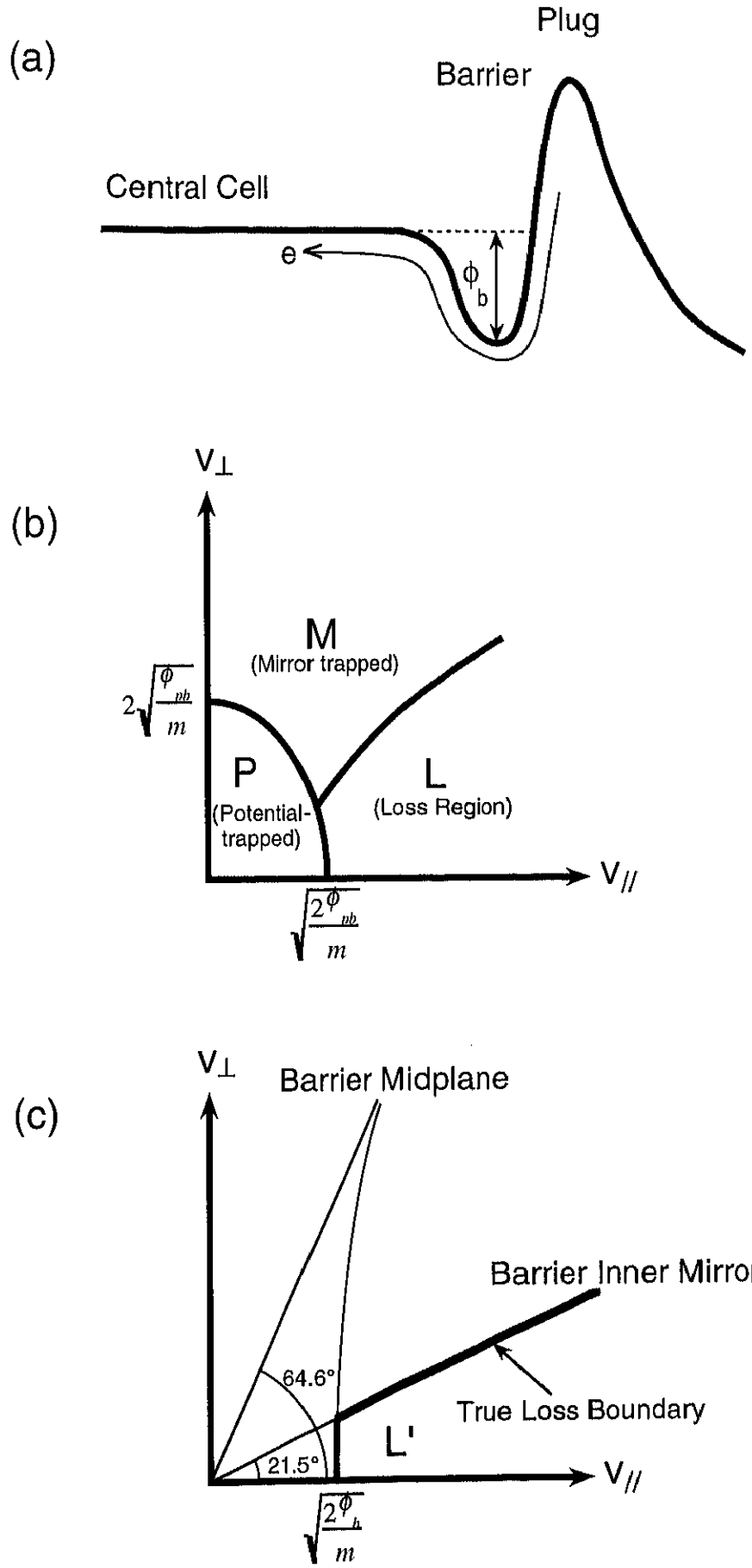
(a)
Plug
Barrier
Central Cell
e
ϕ_b
(b)
$V_\perp$
M
(Mirror trapped)
$2\sqrt{\frac{\phi_{mb}}{m}}$
P
(Potential-trapped)
L
(Loss Region)
$V_{//}$
$\sqrt{\frac{2\phi_{mb}}{m}}$
(c)
$V_\perp$
Barrier Midplane
Barrier Inner Mirror
64.6°
True Loss Boundary
L'
21.5°
$V_{//}$
$\sqrt{\frac{2\phi_b}{m}}$

Fig. 4-4

Electron Loss Boundary

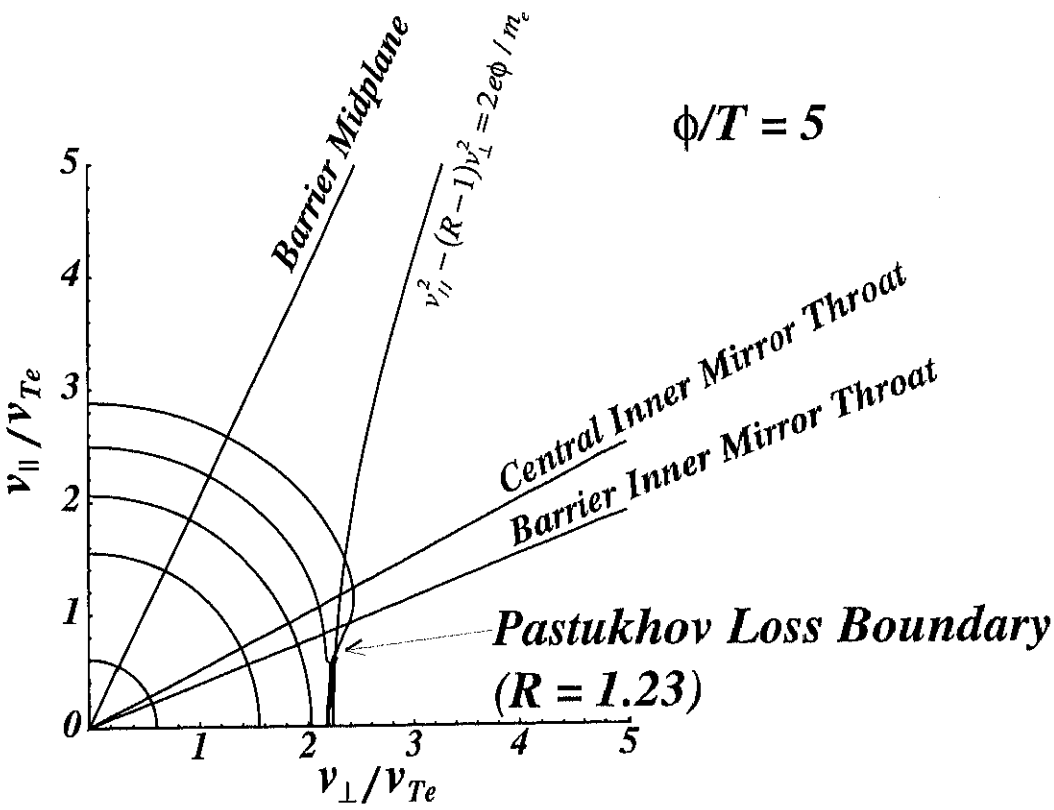

Fig. 4-5

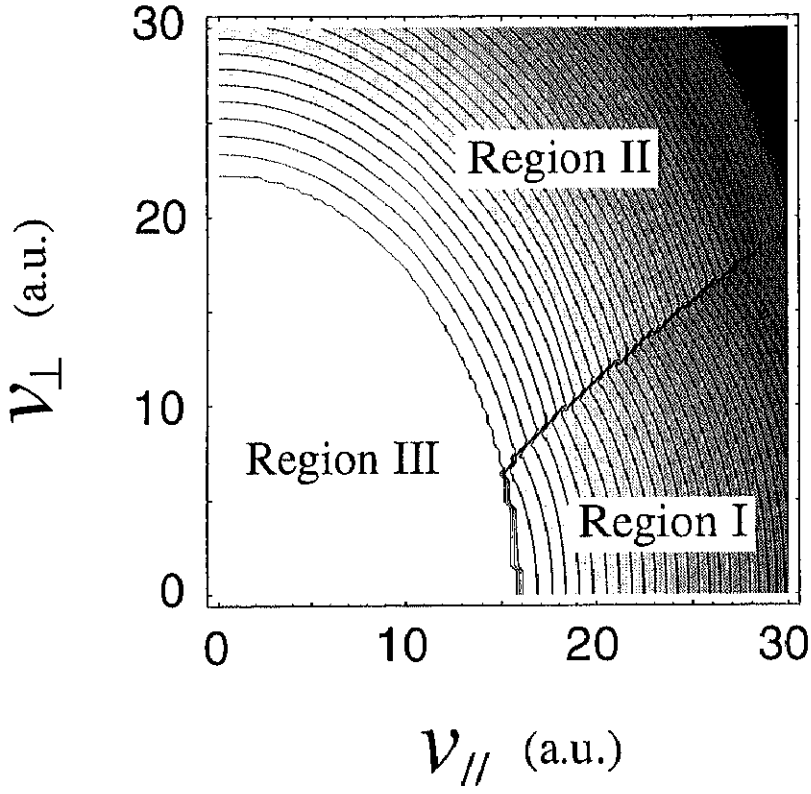

$\Phi_c = 0.4$ kV
$\phi_c = 0.4$ kV
$\phi_b = 0.3$ kV
$T_e = 0.1$ keV

Fig. 4-6

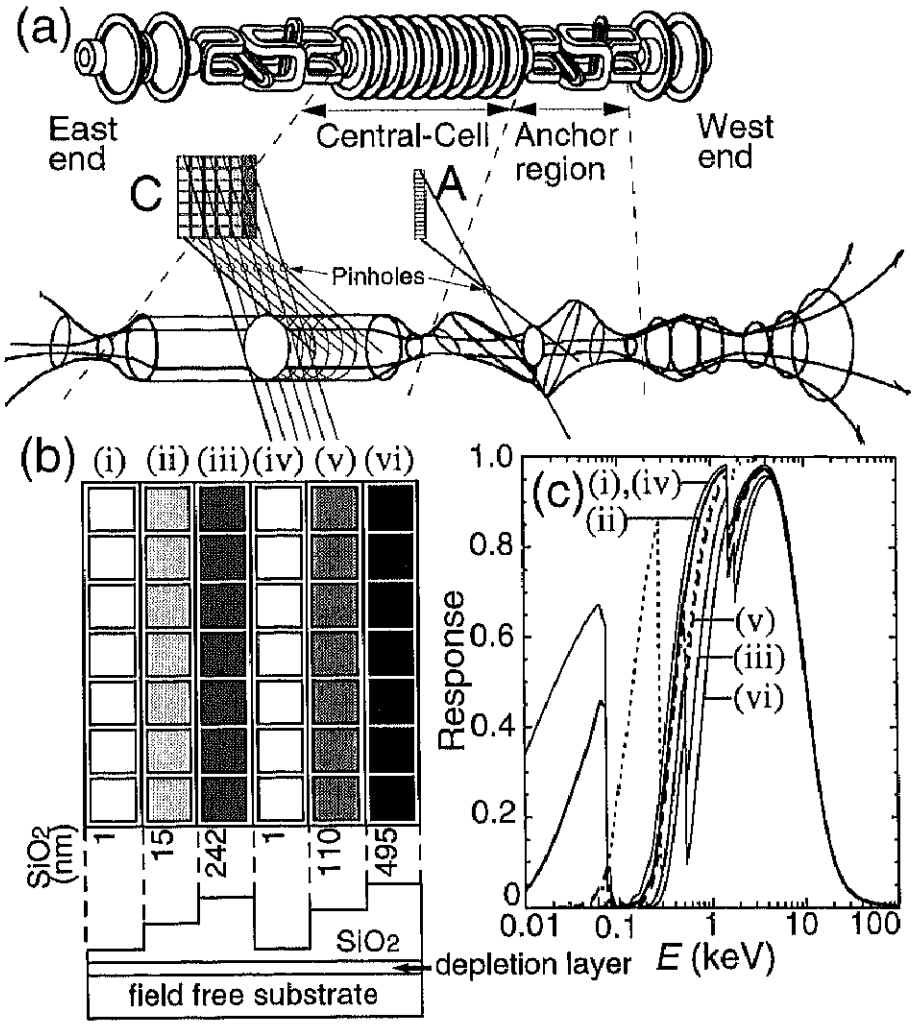
(a)
East end
Central-Cell
Anchor region
West end
C
A
Pinholes
(b)
(i) (ii) (iii) (iv) (v) (vi)
SiO2 (nm)
1
15
242
1
110
495
SiO2
field free substrate
depletion layer
(c)
(i),(iv)
(ii)
(v)
(iii)
(vi)
Response
1.0
0.8
0.6
0.4
0.2
0
0.01
0.1
1
10
100
E (keV)

Fig. 5-1

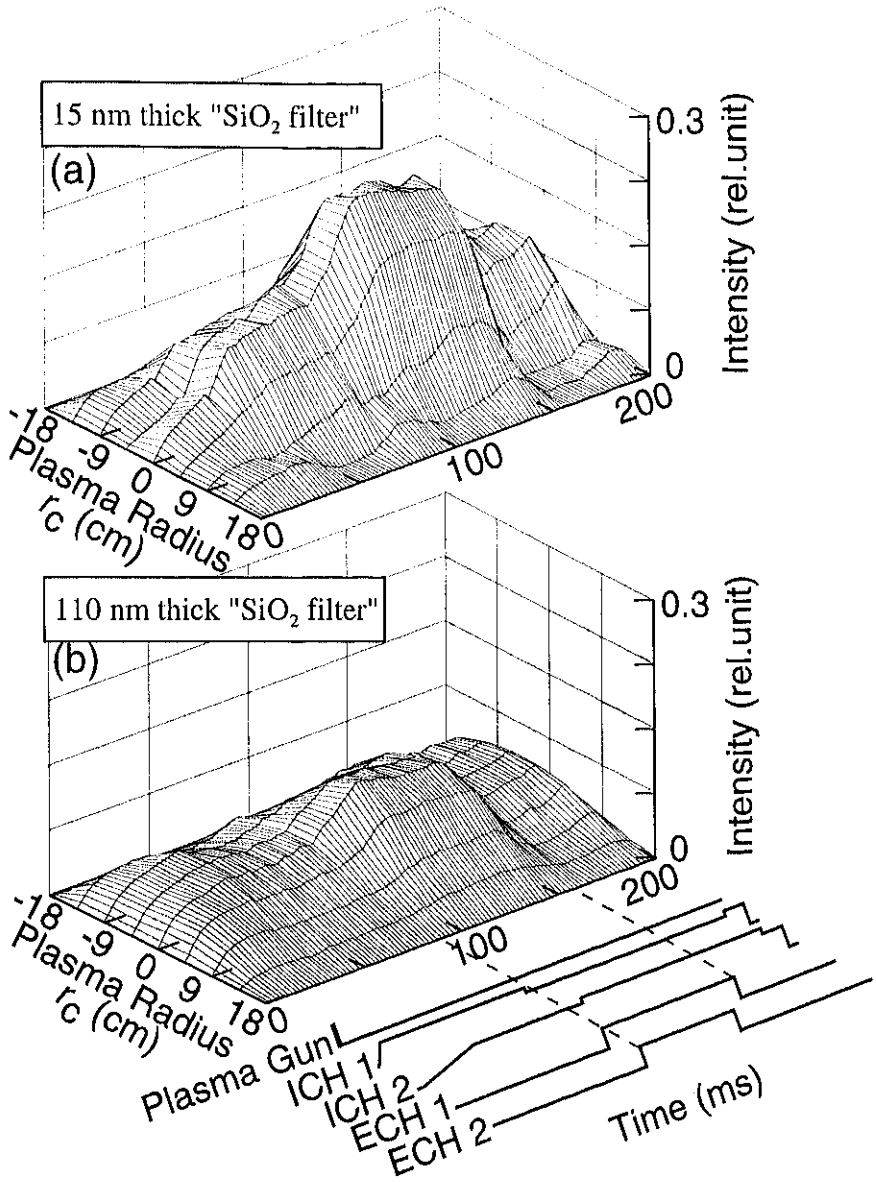
15 nm thick "SiO2 filter"
(a)
0.3
0
Intensity (rel.unit)
-18
-9
0
9
18
Plasma Radius
rc (cm)
100
200
110 nm thick "SiO2 filter"
(b)
0.3
0
Intensity (rel.unit)
-18
-9
0
9
18
Plasma Radius
rc (cm)
100
200
Plasma Gun
ICH 1
ICH 2
ECH 1
ECH 2
Time (ms)

Fig. 5-2

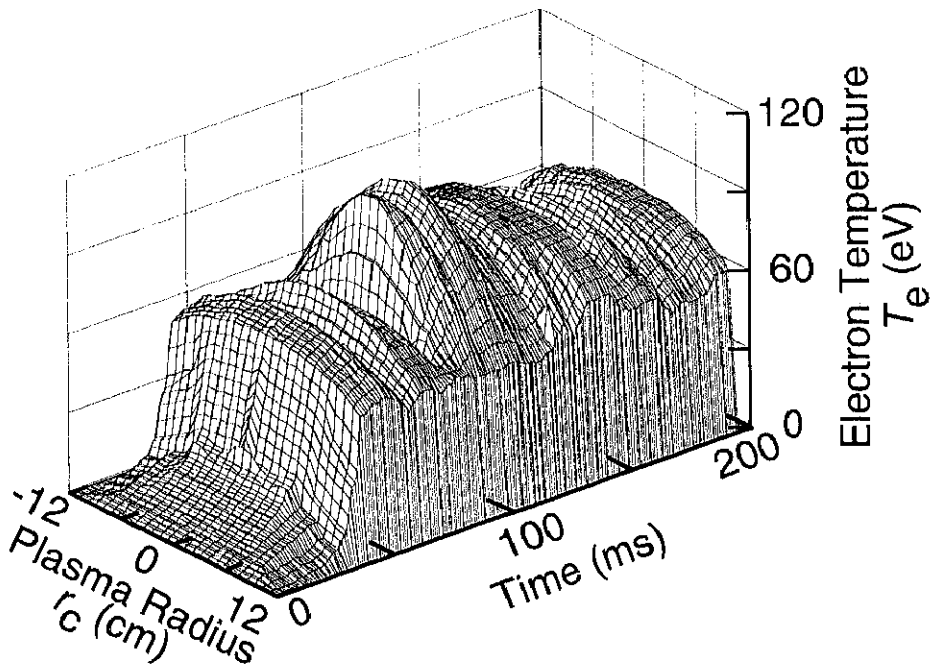
120
60
0
Electron Temperature
T_e (eV)
-12
0
12
Plasma Radius
r_c (cm)
0
100
200
Time (ms)

Fig. 5-3

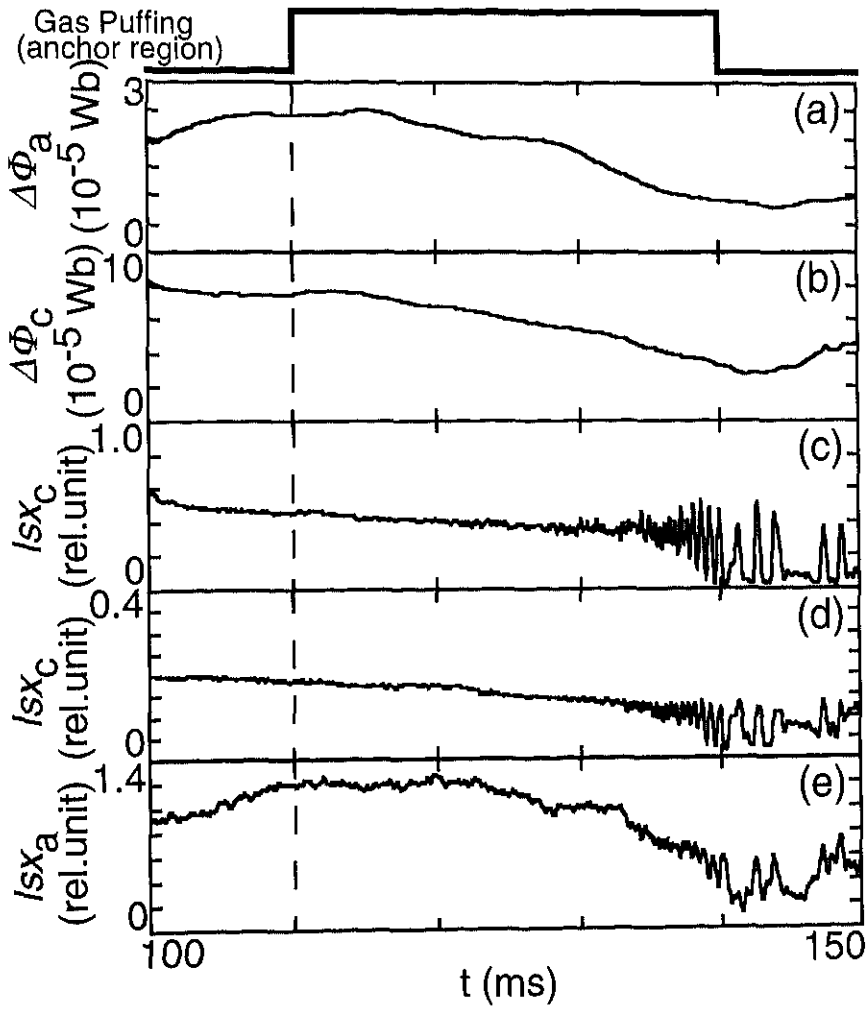
Gas Puffing
(anchor region)
$\Delta\Phi_a$ (10^{-5} Wb)
3
0
(a)
$\Delta\Phi_c$ (10^{-5} Wb)
10
0
(b)
Isx_c (rel.unit)
1.0
0
(c)
Isx_c (rel.unit)
0.4
0
(d)
Isx_a (rel.unit)
1.4
0
(e)
100
150
t (ms)

Fig. 6-1

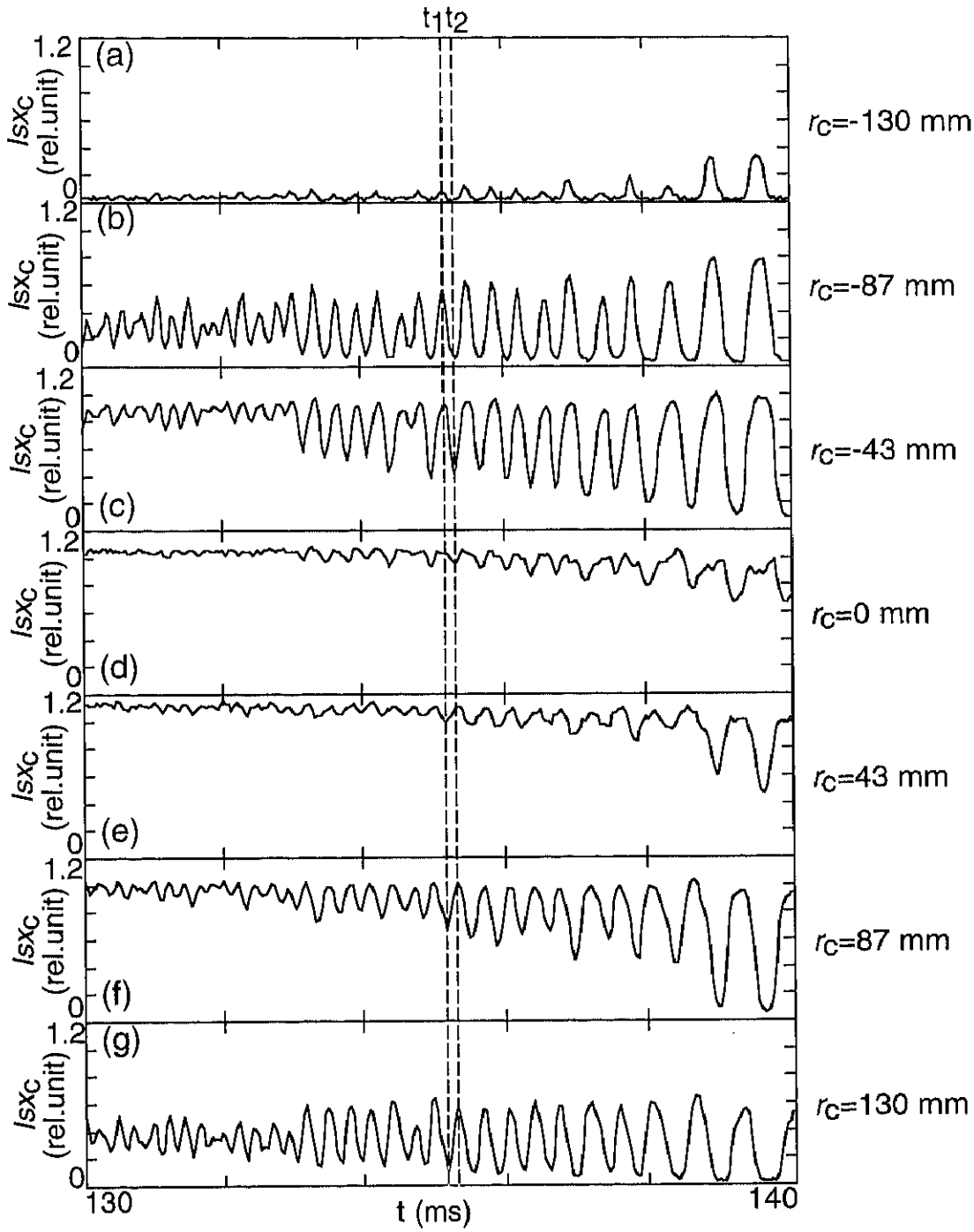
t1t2
(a)
(b)
(c)
(d)
(e)
(f)
(g)
1.2
0
Isxc (rel.unit)
rc=-130 mm
rc=-87 mm
rc=-43 mm
rc=0 mm
rc=43 mm
rc=87 mm
rc=130 mm
130
140
t (ms)

Fig. 6-2

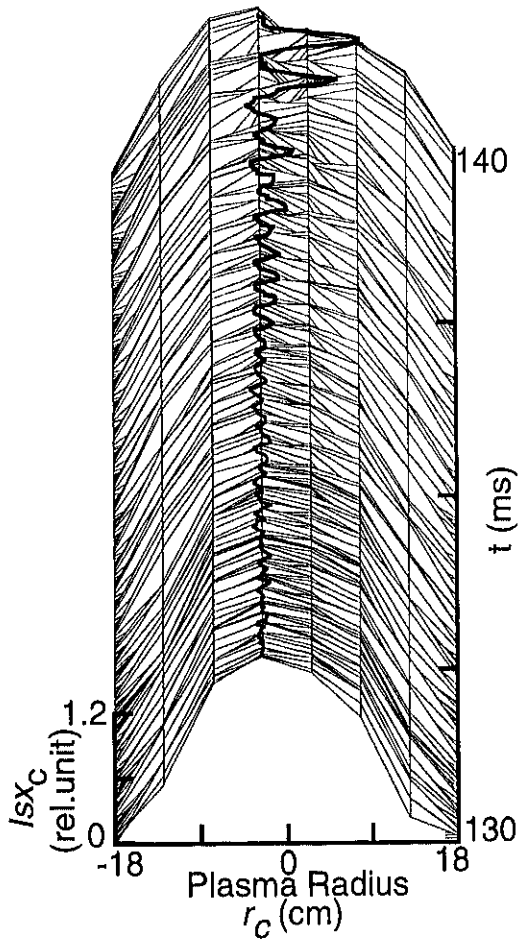

Fig. 6-3

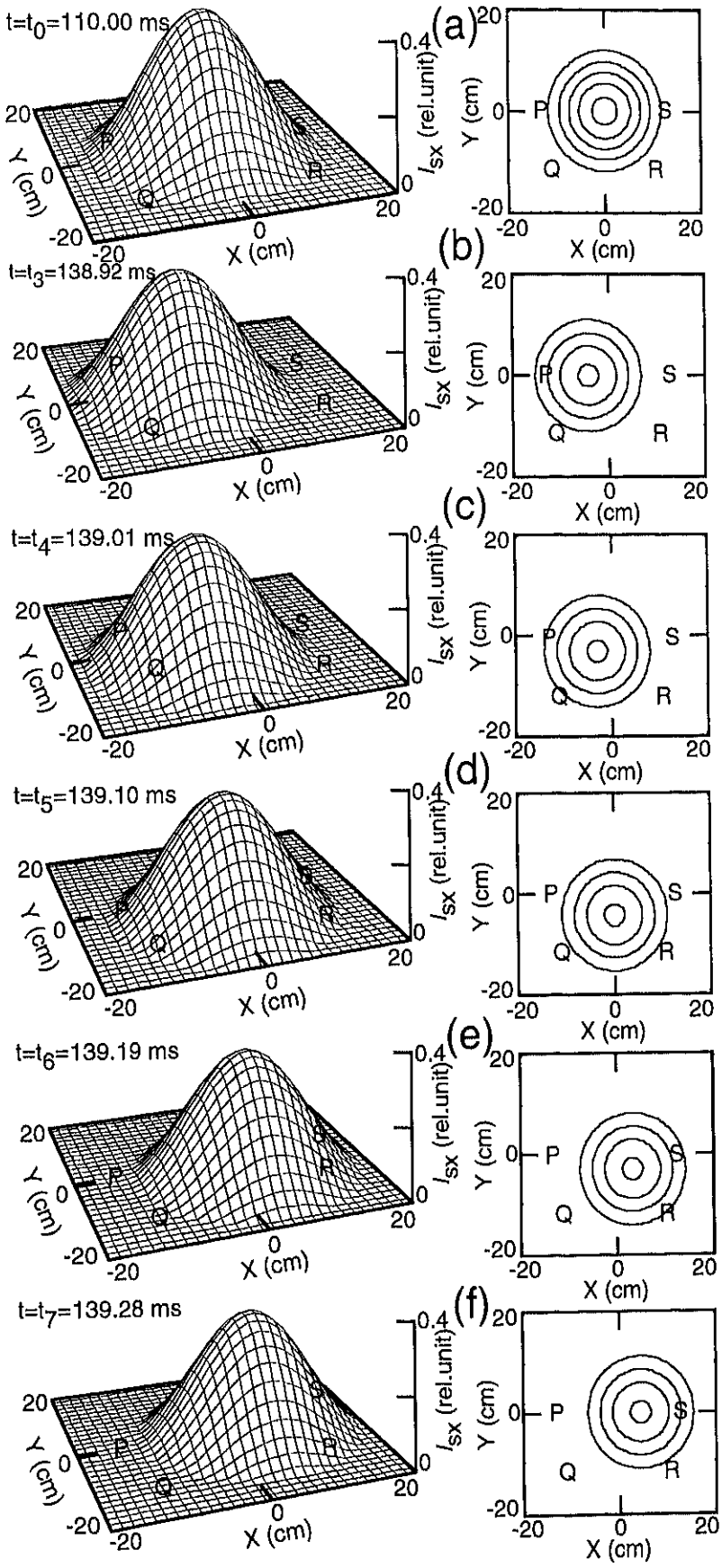
t=t0=110.00 ms
(a)
t=t3=138.92 ms
(b)
t=t4=139.01 ms
(c)
t=t5=139.10 ms
(d)
t=t6=139.19 ms
(e)
t=t7=139.28 ms
(f)
P
Q
R
S
X (cm)
Y (cm)
Isx (rel.unit)
20
0
-20
0.4

Fig. 6-4

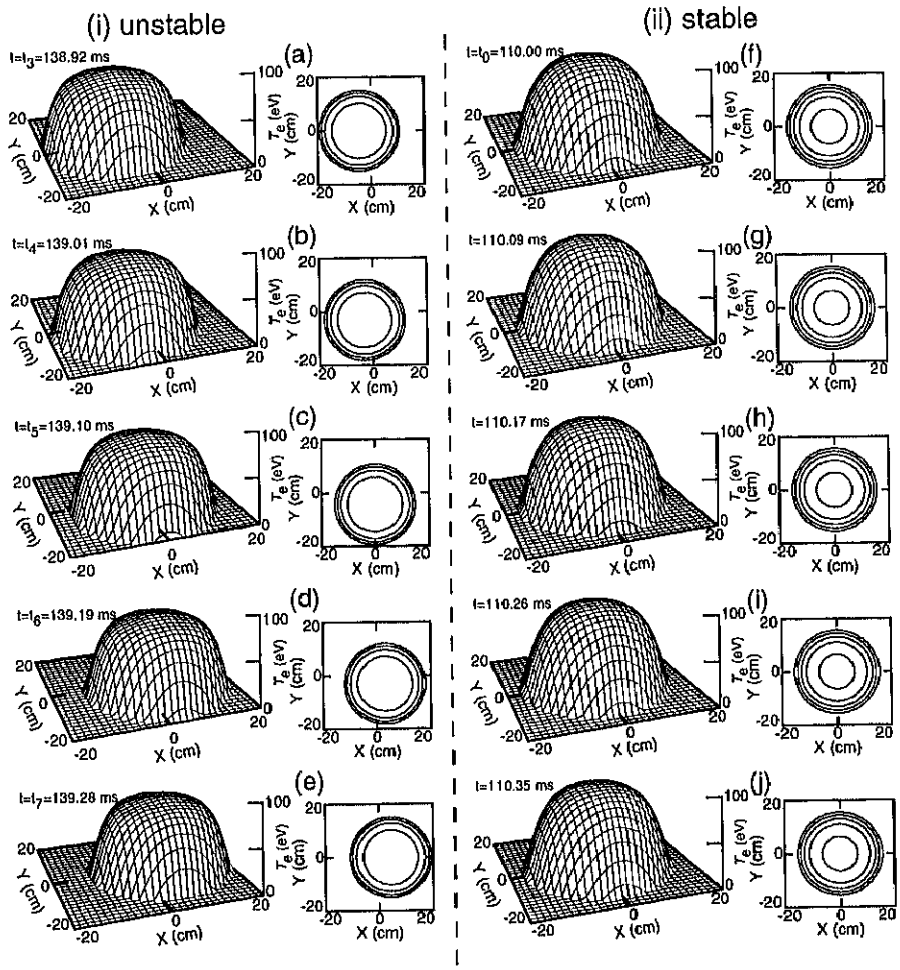
(i) unstable
(ii) stable
t=t3=138.92 ms
(a)
t=t4=139.01 ms
(b)
t=t5=139.10 ms
(c)
t=t6=139.19 ms
(d)
t=t7=139.28 ms
(e)
t=t0=110.00 ms
(f)
t=110.09 ms
(g)
t=110.17 ms
(h)
t=110.26 ms
(i)
t=110.35 ms
(j)
X (cm)
Y (cm)
Te (eV)

Fig. 6-5

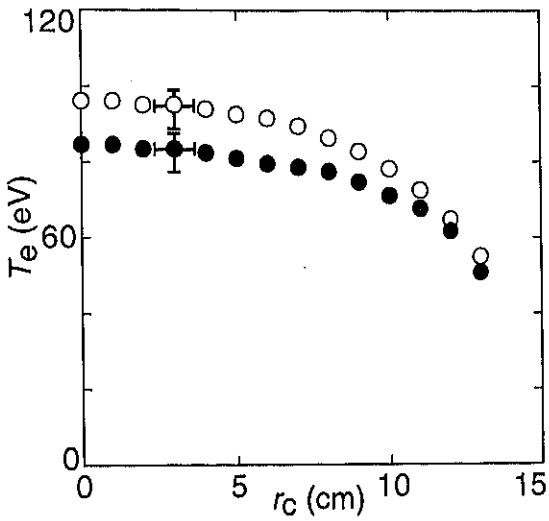

Fig. 6-6

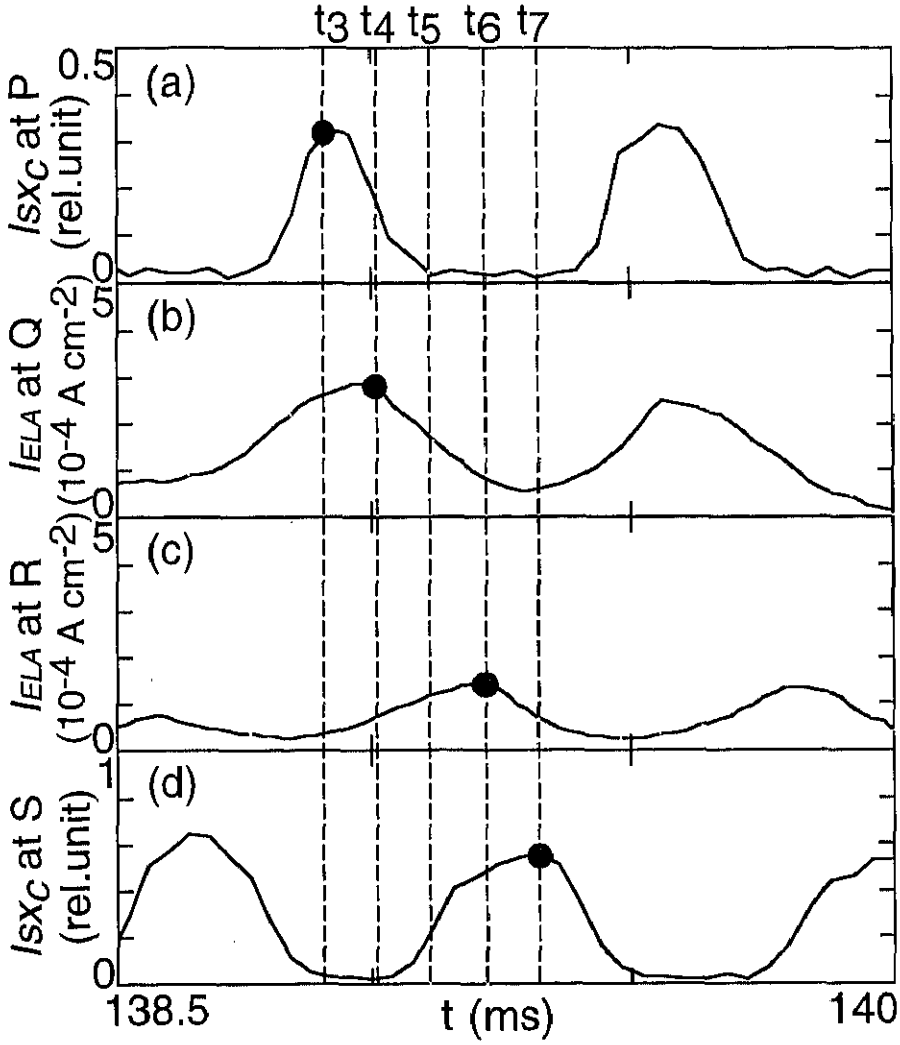
t3 t4 t5 t6 t7
(a)
Isxc at P (rel.unit)
0.5
0
(b)
IELA at Q (10-4 A cm-2)
5
0
(c)
IELA at R (10-4 A cm-2)
5
0
(d)
Isxc at S (rel.unit)
1
0
138.5
t (ms)
140

Fig. 6-7

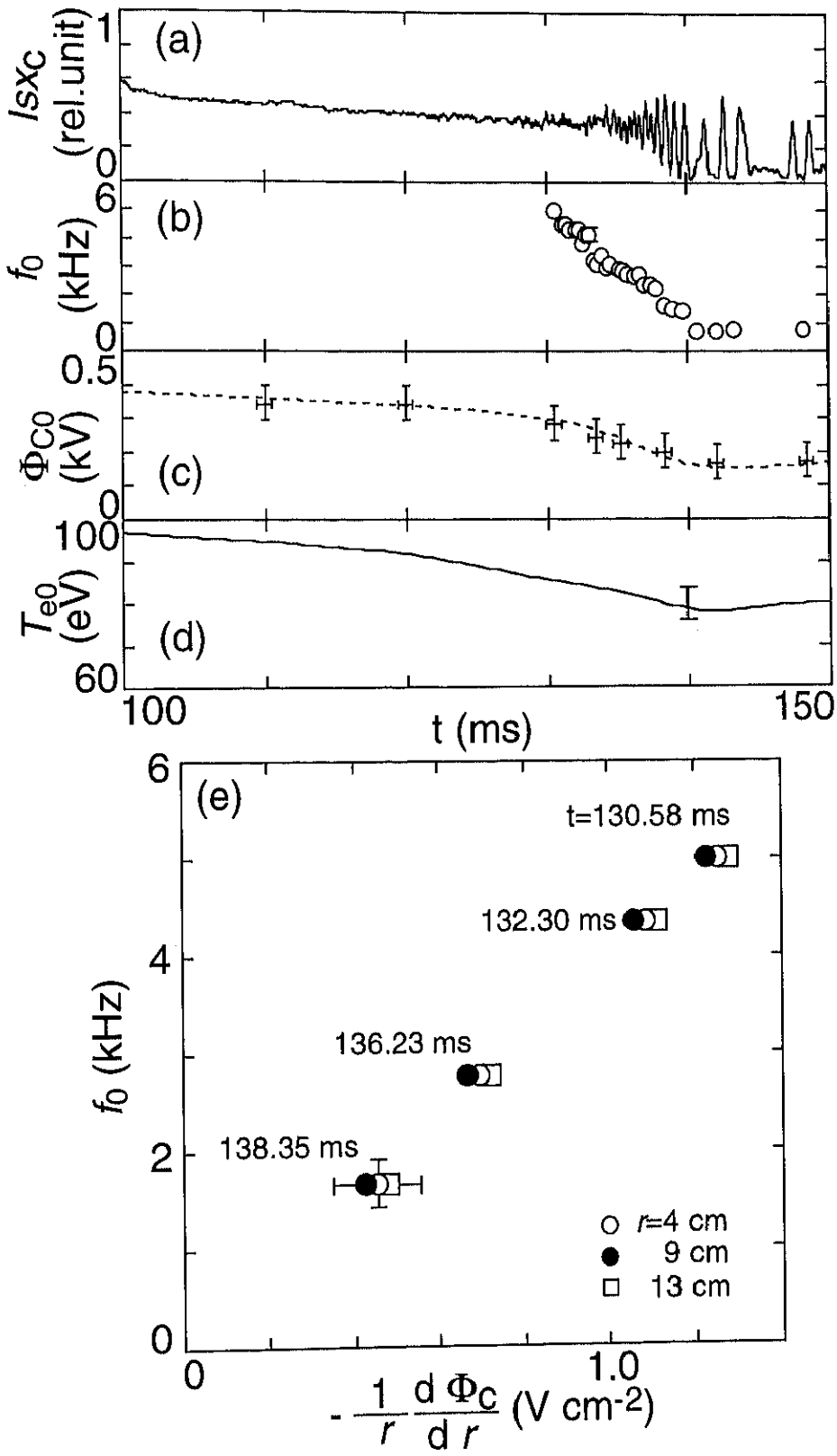
(a)
I_{SXC} (rel.unit)
1
0
(b)
f_0 (kHz)
6
0
(c)
Φ_{C0} (kV)
0.5
0
(d)
T_{e0} (eV)
100
60
100
150
t (ms)
(e)
t=130.58 ms
132.30 ms
136.23 ms
138.35 ms
f_0 (kHz)
6
4
2
0
r=4 cm
9 cm
13 cm
0
1.0
$-\frac{1}{r}\frac{d\Phi_C}{dr}$ (V cm^{-2})

Fig. 6-8

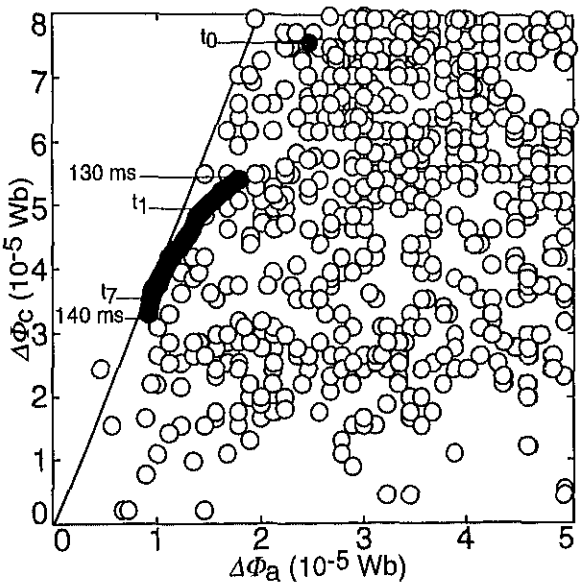

Fig. 6-9

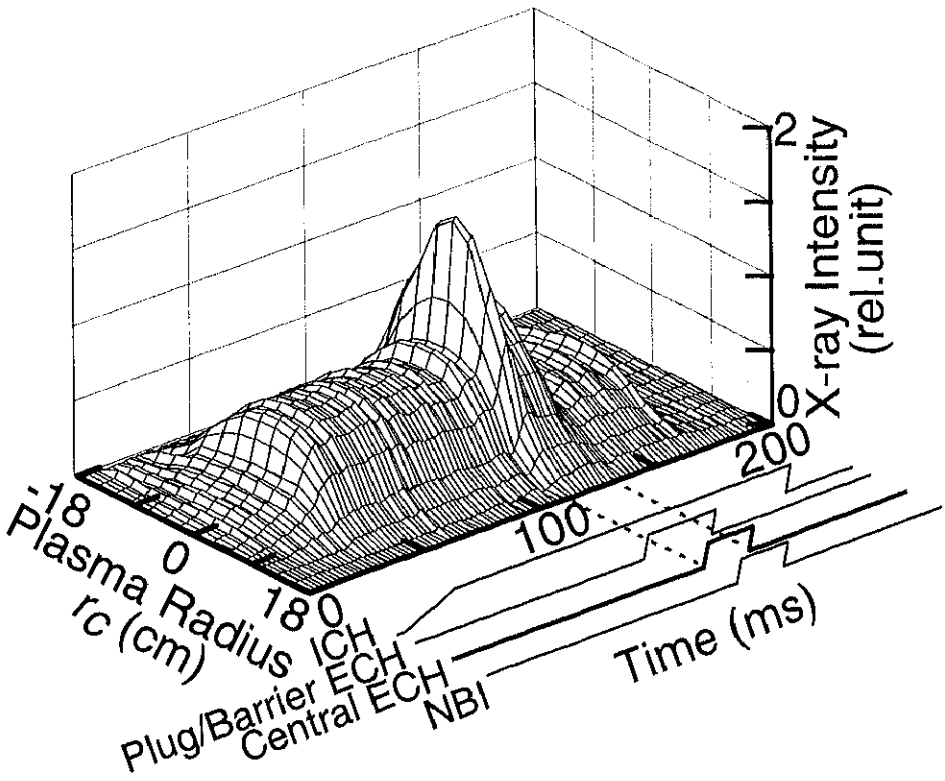
2
X-ray Intensity
(rel.unit)
0
200
100
Time (ms)
-18
0
18
Plasma Radius
rc (cm)
0
ICH
Plug/Barrier ECH
Central ECH
NBI

Fig. 6-10

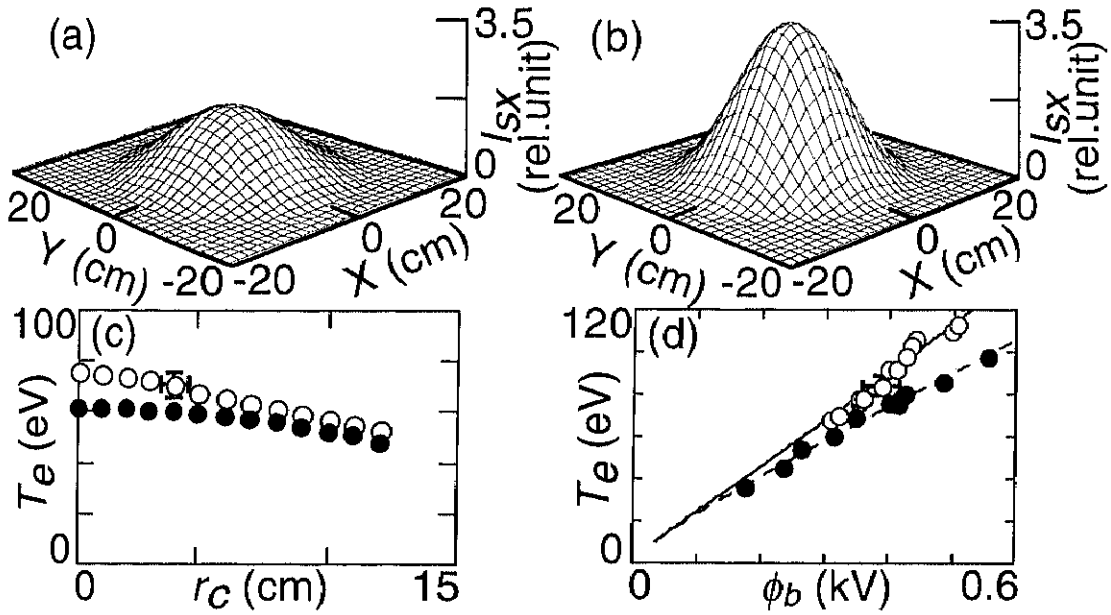
(a)
3.5
0
I_{SX} (rel.unit)
20
0
Y (cm)
-20
-20
0
X (cm)
20
(b)
3.5
0
I_{SX} (rel.unit)
20
0
Y (cm)
-20
-20
0
X (cm)
20
100
(c)
T_e (eV)
0
0
r_c (cm)
15
120
(d)
T_e (eV)
0
0
ϕ_b (kV)
0.6

Fig. 6-11